In vitro studies of Fe3O4 ZIF 8 core–shell nanoparticles designed as potential theragnostics

Romy Ettlinger, Natalia Moreno, Natalia Ziółkowska, Aladin Baldur Bernd Ullrich, Hans-Albrecht Krug von Nidda, Daniel Jirák, Kornelius Kerl, Hana Bunzen

In Vitro Studies of Fe₃O₄-ZIF-8 Core–Shell Nanoparticles Designed as Potential Theragnostics

Romy Ettlinger, Natalia Moreno, Natalia Ziółkowska, Aladin Ullrich, Hans-Albrecht Krug von Nidda, Daniel Jirák, Kornelius Kerl,* and Hana Bunzen*

Theragnostics represent a combination of therapy and diagnosis within one system. Herein, Fe_3O_4-ZIF-8 core–shell nanoparticles are developed and suggested as candidates for theragnostic applications in cancer treatment. A drug loaded metal–organic framework ZIF-8 (zeolitic imidazolate framework-8) represents the therapeutic tool, while the Fe_3O_4 core is included to enable the material visualization by magnetic resonance imaging (MRI). A reliable synthesis of Fe_3O_4-ZIF-8 core–shell nanoparticles of an average size below 100 nm is reported. The nanoparticles are characterized by FT-IR, TGA, XRPD, TEM, STEM-EDS, DLS, ICP-OES, CHN-elemental analysis, SQUID measurements, and MRI. Moreover, their chemical stability and in vitro cytotoxicity against fibroblast and selected cancer cell lines are evaluated. As a model drug, arsenic trioxide—a promising anticancer drug—is used. The drug release can be triggered by a pH change from 7.4 to 6.0 and the nanoparticles can be visualized by MRI in vitro, thus a potential theragnostic agent for cancer treatment is developed.

1. Introduction

Theragnostics represent a new highly promising field in medicine.[1–4] They combine *thera*py and diag*nosis* within one system. Integrating diagnostic information with pharmaceuticals is highly attractive because it simultaneously provides a more targeted, efficient patient treatment and reduction of clinical costs and resources.[4,5] Especially in the treatment of oncological diseases, where novel therapeutic approaches are urgently needed, the seamless connection of therapy, diagnosis, and treatment response via one single system is considered to be a major step forward.[1–3] For the diagnostic part, various agents have been suggested including superparamagnetic iron oxide nanoparticles (SPIOs) which can be used as contrast agents in magnetic resonance imaging (MRI).[6] SPIOs feature a good biocompatibility and low-toxicity, and are superparamagnetic (for particle sizes equal or smaller than one single magnetic domain, i.e., <25 nm).[7] Moreover, when combined with drug delivery, theragnostics are prepared.[8–10] Whereas, their performance as MRI contrast agent is outstanding, their drug loading capacity is limited since the drug can be attached only onto the nanoparticle surface. Therefore, various coatings have been suggested to enlarge the drug loading capacity of Fe_3O_4 nanoparticles. These include coating with various polymers,[11,12] mesoporous silica,[13,14] or graphene oxide.[15] Especially, the attempts with the mesoporous silica coating yielded nanoparticles with high drug loading.[13,14] To increase the loading capacity even more and to introduce some additional features such as stimuli-responsivity and biodegradability, we propose to combine Fe_3O_4 nanoparticles with metal–organic frameworks (MOFs).

R. Ettlinger, Dr. H. Bunzen
Chair of Solid State and Materials Chemistry
Institute of Physics
University of Augsburg
Universitätsstraße 1, Augsburg D-86159, Germany
E-mail: hana.bunzen@physik.uni-augsburg.de

Dr. N. Moreno, Dr. K. Kerl
Pediatric Hematology and Oncology
University Children's Hospital Muenster
Albert-Schweitzer-Campus 1, Muenster D-48149, Germany
E-mail: Kornelius.Kerl@ukmuenster.de

N. Ziółkowska, Dr. D. Jirák
First Faculty of Medicine
Institute of Biophysics and Informatics
Charles University
Salmovská 1, Prague 120 00, Czech Republic

Dr. A. Ullrich
Chair of Experimental Physics IV
Institute of Physics
University of Augsburg
Universitätsstraße 1, Augsburg D-86159, Germany

Dr. H.-A. Krug von Nidda
Chair of Experimental Physics V
Centre for Electronic Correlations and Magnetism
Institute of Physics
University of Augsburg
Universitätsstraße 1, Augsburg D-86159, Germany

Dr. D. Jirák
Department of Diagnostic and Interventional Radiology
Institute for Clinical and Experimental Medicine
Vídeňská1958/9, Prague 4 140 21, Czech Republic

**ADVANCED
SCIENCE NEWS**
www.advancedsciencenews.com

Particle
& Particle Systems Characterization
www.particle-journal.com

MOFs represent crystalline porous coordination polymers, which consist of inorganic metal ions (or clusters) and organic ligands.[16] Due to their outstanding properties such as high internal surface area and chemical and design versatility,[17,18] MOFs have been suggested for various applications including gas storage and separation,[19,20] catalysis,[21–23] and also medicine.[24–26] For instance, ZIF-8 (Zeolitic imidazolate framework-8), composed of Zn ions and imidazolate ligands,[27] has been considered as a promising drug delivery system due to its high porosity and suitable pH-sensitive degradation.[28,29] There have been also reports on combining MOFs with magnetic nanoparticles, but this has been done mainly for catalysis[30,31] and extraction applications.[32,33] Up to now there have been only few examples of Fe_3O_4-MOFs for medicinal applications[26,34–38] and in these cases if core–shell nanoparticles have been prepared,[26,34–36] they have been larger than 180 nm which is not optimal when an intravenous drug distribution is intended.[39]

As a model drug, we selected arsenic trioxide (ATO). ATO has been approved for the treatment of acute promyelocytic leukemia (APL) by the U.S. Food and Drug Administration (FDA) in 2000[40] and by the European Medicines Agency (EMA) in 2016.[41] These approvals promoted further research of utilizing ATO and other arsenic compounds in cancer therapy including the treatment of solid tumor entities, such as breast cancer,[42] cervical cancer,[43] or even brain tumors.[44] Unfortunately, it turned out that the treatment of solid tumors is very challenging. Due to the arsenic toxicity, the increase of dosage is limited, and thus the drug enrichment in the tumor is often insufficient. To solve this issues, using nanocarriers has been suggested.[40,45] So far only few materials have been tested for preparing delivery systems of arsenic drugs. These include liposomes, polymeric micelles, or mesoporous silica nanoparticles.[45] Recently we also contributed to the field by developing MOF based nanocarriers for ATO delivery.[46–48] In this work, we focused on developing a theragnostic agent for delivery of arsenic trioxide.

2. Results and Discussion

2.1. Material Synthesis and Drug Loading

2.1.1. Fe₃O₄ Nanoclusters

In the reported examples of Fe_3O_4-MOFs,[34–36] the overall nanoparticle size was larger than 180 nm and the major part of the nanocomposite was formed by the Fe_3O_4 core and there was only a thin MOF shell. This is not optimal regarding the potential theragnostic applications since it seriously limits the drug loading capacity. Moreover, if intravenous distribution is intended, smaller nanoparticle sizes are preferred.[39] Therefore, the size of the Fe_3O_4 core had to be scaled down significantly.

Fe_3O_4 nanoclusters featuring superparamagnetic behavior and an overall particle size below 50 nm were synthetized by combining $FeCl_3 \cdot 6H_2O$, sodium acetate, and trisodium citrate, and heating them in a mixture of diethylene glycol and ethylene glycol. We discovered that the absence of water and the ratio of diethylene glycol and ethylene glycol were the crucial factors to control the cluster size. Furthermore, the addition
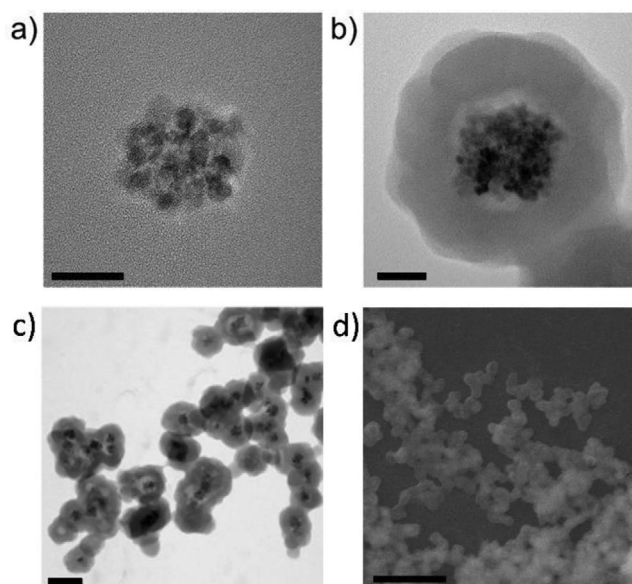
Figure 1. HR TEM micrographs of a) Fe_3O_4 nanoclusters, b,c) PEG-NH₂@ Fe_3O_4-ZIF-8 nanoparticles, and d) a SEM micrograph of PEG-NH₂@ Fe_3O_4-ZIF-8 nanoparticles; scale bar: (a,b) 20 nm, (c) 100 nm, (d) 1 μm.

of citrate and acetate to the reaction mixture resulted in highly hydrophilic superparamagnetic nanoparticle clusters. The analysis of the Fe_3O_4 nanoclusters by transmission electron microscopy (TEM) revealed that the size of a single nanoparticle was around 6.4 ± 0.8 nm, while the total nanoparticle cluster size was around 35.1 ± 4.5 nm (TEM, **Figure 1** and Figure S2, Supporting Information, calculated for 100 nanoparticles). A hydrodynamic diameter determined by dynamic light scattering (DLS) in water was 72.7 nm with a polydispersity index (PDI) of 0.194 (Figure S5, Supporting Information).

2.1.2. Fe₃O₄-ZIF-8 Nanoparticles

The growth of ZIF-8 around the Fe_3O_4 nanoclusters was optimized with a special attention paid to the solvent choice. On the one hand the Fe_3O_4 nanoclusters have to be homogeneously dispersed (i.e., water as solvent is preferred), on the other hand a moderate growth speed of the MOF shell is needed to ensure the actual growth onto the surface of the Fe_3O_4 nanoclusters and not only alongside (i.e., methanol as solvent is preferred). For details, see Figure S1 (Supporting Information). In the optimized synthesis, the Fe_3O_4 nanoclusters were dispersed in a mixture of water and methanol, and then the linker (2-methylimidazole) dissolved in methanol was added. Subsequently, the Zn(II) ions (dissolved in a mixture of water and methanol) were added, and the synthesis was carried out at room temperature. Optimal reaction conditions were determined to be 30 min of reaction time and 15 min of separation by applying an external magnetic field. To improve the nanoparticle biocompatibility, the surface of the nanoparticles was coated with polyethylene glycol—a polymer with a widespread use in biomedicine.[8] We used an amino-functionalized derivative of polyethylene glycol (PEG-NH₂, MW 5516 Da) to enable coordinate interactions between the amino end-groups of the

polymer and zinc centers of the MOF, in a way that the polymer is bound to the surface and a penetration into the pores of the framework is hindered.[49] As a result, core–shell nanoparticles of overall particle sizes around 97 ± 8 nm as determined by TEM (Figure 1, Figures S2–S4, Supporting Information, calculated for 100 nanoparticles) were obtained. A hydrodynamic diameter of these nanoparticles determined by DLS in water was 214.5 nm with a polydispersity index (PDI) of 0.213 (Figure S5, Supporting Information).

2.1.3. Drug Loading

To load the core–shell nanoparticles with arsenic trioxide, we used sodium (meta)arsenite ($NaAsO_2$) as the drug precursor. $NaAsO_2$ is highly soluble in water, and thus a highly concentrated drug solution could be used. The pH value of the aqueous solution was adjusted to pH 7 to generate $As(OH)_3$. The Fe_3O_4-ZIF-8 nanoparticles were kept in the solution at room temperature for 2 h. The surface of the drug loaded nanoparticles was coated by PEG-NH_2 following the same procedure as for the drug free nanoparticles.

2.1.4. Material Characterization

The polymer coated samples (denoted as PEG-NH_2@Fe_3O_4-ZIF-8 and PEG-NH_2@As@Fe_3O_4-ZIF-8) were characterized by FT-IR (**Figure 2**a and Figure S6, Supporting Information) and XRPD (Figure 2b) to verify that they comprised both Fe_3O_4 and ZIF-8. In their FT-IR spectra, besides the characteristic bands of ZIF-8, bands at 590, 640, and a broadening at 1600 cm^{-1} were found, which corresponded to the bands of the carboxylate-capped Fe_3O_4 nanoclusters.[50] Furthermore, bands at 840, 1100, 1250, and 2870 cm^{-1}, which corresponded to C–H bending vibrations, O–H and C–O–H stretching vibrations of the PEG-NH_2-coating, were detected.[49] The successful polymer coating was further confirmed by thermogravimetric analysis, which revealed that 6.1 wt% of PEG-NH_2 coating were present (Figure S7, Supporting Information). Additionally, the visualization of the nanoparticles by TEM confirmed that the core–shell type of structure was retained after the drug loading and surface modification (Figure 1 and Figure S2, Supporting Information).
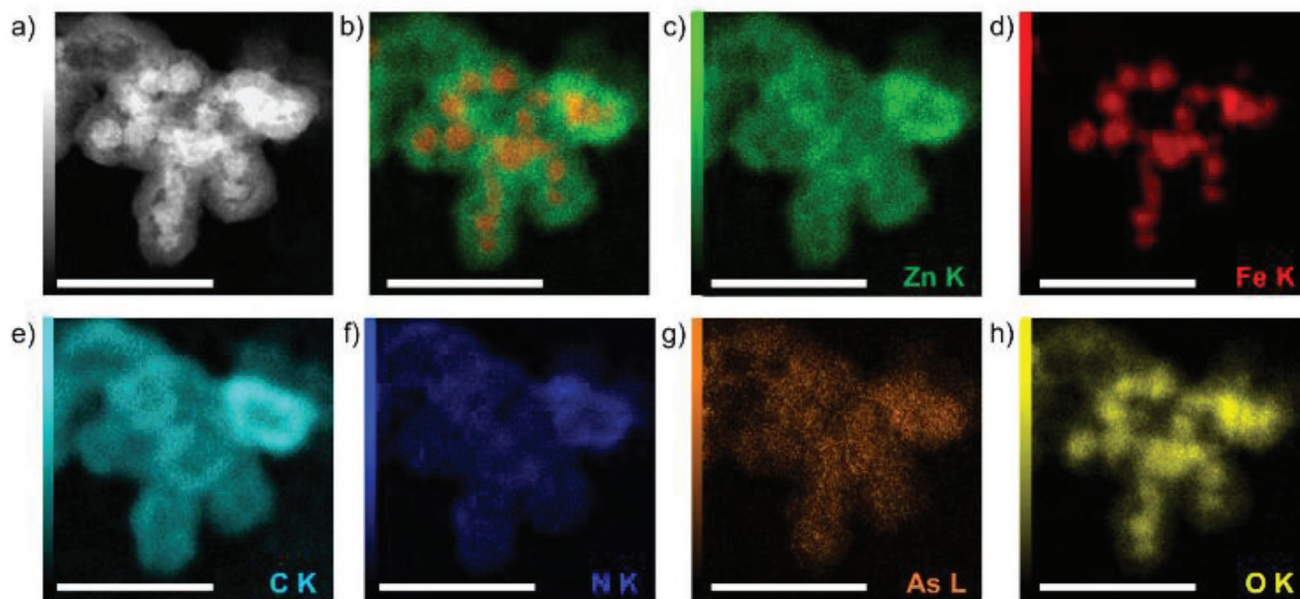
The successful drug loading was confirmed by FT-IR spectroscopy. ATO is bound to the structure of ZIF-8 [$Zn(C_4N_2H_5)_2$] in a form of arsenite anions ($H_2AsO_3^-$) via a post-synthetic ligand exchange.[48] Due to the exchange, new bands were detected at 360, 550, 660, and 710 cm^{-1} (Figure 2a), which corresponded to the As–OH bending, the symmetric and asymmetric mode of stretching vibrations of $As(OH)_2$ and As–O.[51] To further validate the exchange of the imidazolate linker to the arsenite ligand, CHN-elemental analysis was carried out (Table S1, Supporting Information). In the drug free Fe_3O_4-ZIF-8 and PEG-NH_2@Fe_3O_4-ZIF-8, the MOF sum formula was found to be $Zn(C_4N_2H_5)_{1.94}$ and $Zn(C_4N_2H_5)_{1.91}$, which corresponds to 0.06 and 0.09 missing linkers per zinc cation, respectively. This deviation can be explained by minor defects in the framework. However, after the loading of arsenite (i.e., in As@Fe_3O_4-ZIF-8 and PEG-NH_2@As@Fe_3O_4-ZIF-8), the number of missing
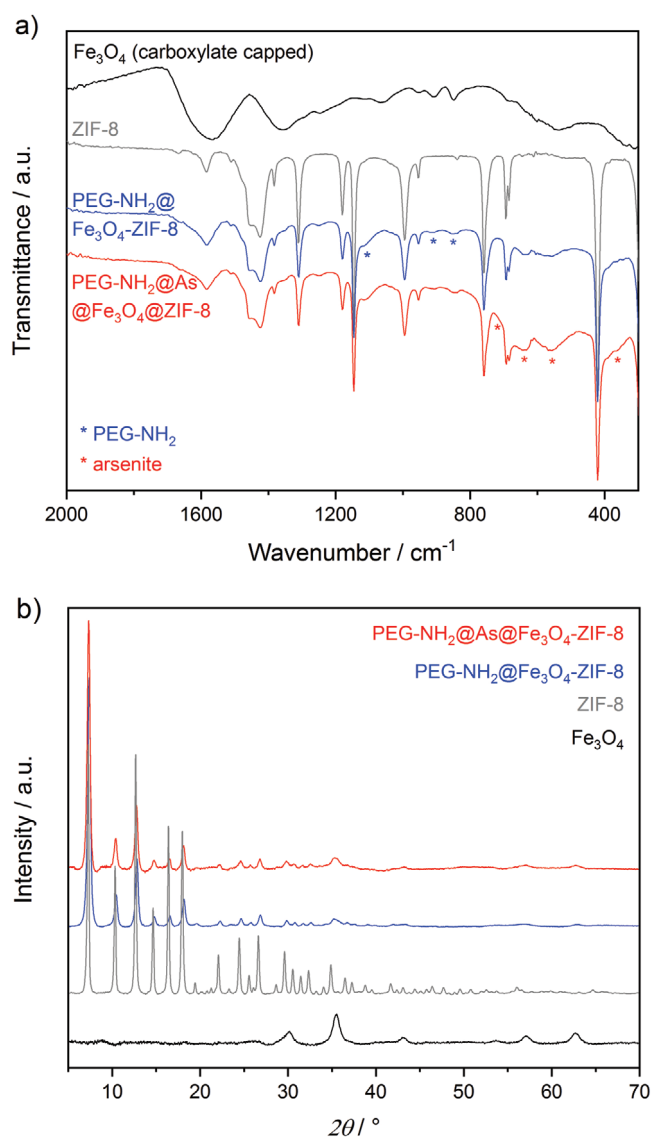
Figure 2. a) FT-IR spectra in the area from 2000 to 300 cm^{-1} and b) XRPD pattern of Fe_3O_4 (black), ZIF-8 (grey), PEG-NH_2@Fe_3O_4-ZIF-8 (blue), and PEG-NH_2@As@Fe_3O_4-ZIF-8 (red).

linkers per zinc atom increased to 0.32 and 0.33 [$Zn(C_4N_2H_5)_{1.68}$ and $Zn(C_4N_2H_5)_{1.67}$], respectively, supporting our finding of the partial replacement of the linker by arsenite. The quantification of the arsenic amount by ICP-OES analysis revealed a ratio of Zn: As to be 1: 0.20 ± 0.02 (average value of three measurements) which corresponded to 53 mg of arsenic in 1 g of material (equivalent to 70 mg of As_2O_3/1 g). To visualize the element distribution, EDS elemental mapping was carried out (**Figure 3** and Figure S4, Supporting Information). The overlay of the elements Fe and Zn in Figure 3b confirmed the core–shell nanoparticle structure by showing the presence of Fe only in the core and Zn in the shell. The EDS elemental mapping also revealed that As was homogeneously distributed within the ZIF-8 shell (Figure 3g). The findings were further supported by the compositional map of the element O (presented in Fe_3O_4 and the drug) showing a high intensity in the same area as Fe

ADVANCED
SCIENCE NEWS
www.advancedsciencenews.com

Particle
& Particle Systems Characterization
www.particle-journal.com

Figure 3. EDS elemental mapping of PEG-NH$_2$@As@Fe$_3$O$_4$-ZIF-8: a) Dark field STEM image, b) an overlay of Zn (green) and Fe (red) compositional maps and the compositional maps of c) Zn (green), d) Fe (red), e) C (light blue), f) N (dark blue), g) As (orange) and h) O (yellow); scale bar: 200 nm.

and being homogeneously distributed within the ZIF-8 shell as the element As.

2.2. Magnetic Properties and Magnetic Resonance Imaging

2.2.1. SQUID Measurement

The magnetic properties of the core–shell nanoparticles were analyzed with a superconducting quantum interference device (SQUID) at room temperature. The magnetization curve $M(H)$ of the PEG-NH$_2$@Fe$_3$O$_4$-ZIF-8 nanoparticles depending on the external magnetic field H is shown in **Figure 4** and is
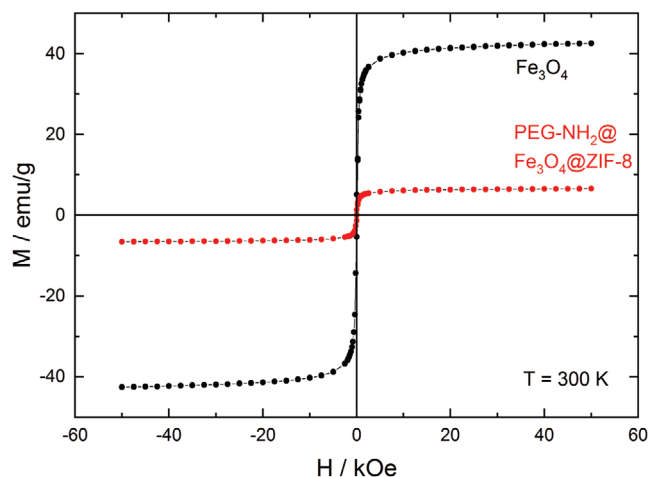

Figure 4. Magnetization loops $M(H)$ of Fe$_3$O$_4$ (black symbols) and PEG-NH$_2$@Fe$_3$O$_4$-ZIF-8 (red symbols) as a function of the external magnetic field H measured at 300 K.

compared to the magnetization curve of the Fe$_3$O$_4$ clusters. For both samples, starting from $M = 0$ at $H = 0$ on increasing field, the magnetization approaches saturation already above 5 kOe and returns to zero on decreasing field without any hysteresis effects and shows analogous behavior for inverse magnetic field. The saturation magnetization of the Fe$_3$O$_4$ nanoclusters was 42.6 emu g^{-1}, i.e., about half of the bulk value,[52] while the magnetization of the PEG-NH$_2$@Fe$_3$O$_4$-ZIF-8 core–shell nanoparticles decreased to 6.6 emu g^{-1}. The decrease in magnetization (expressed in emu g^{-1}) can be attributed to the increase of the overall material mass when PEG-NH$_2$@Fe$_3$O$_4$-ZIF-8 compared to carboxylate capped Fe$_3$O$_4$. This finding is in good agreement with data reported for similar materials such as ZIF-8/cellulose/Fe$_3$O$_4$ nanocomposites.[53] Since both samples showed no magnetization in the absence of an external magnetic field and no hysteresis effects, their expected superparamagnetic behavior could be confirmed.

2.2.2. MR Imaging and Relaxometry

We investigated the performance of the Fe$_3$O$_4$ nanoclusters, drug free PEG-NH$_2$@Fe$_3$O$_4$-ZIF-8 and drug loaded PEG-NH$_2$@As@Fe$_3$O$_4$-ZIF-8 nanoparticles as MRI contrast agents. The nanoparticles were mixed in agar to suppress their possible sedimentation. The tested concentration range was from 0.1 to 1.5×10^{-3} M (calculated for the iron content). The phantoms were visible as hypointense regions, both in T$_1$ and T$_2$ weighted MR images, for all tested Fe-concentrations and all the results are summarized in **Figure 5**, including the fractional signal loss (FSL), signal-to-noise ratio (SNR) and contrast-to-noise ratio (CNR). Additionally, the relaxation times T$_1$ and T$_2$ of all three materials were also evaluated and the calculated r_1 and r_2 and r_2/r_1 ratios are shown in **Table 1**. The resulting r_2/r_1 ratio of the
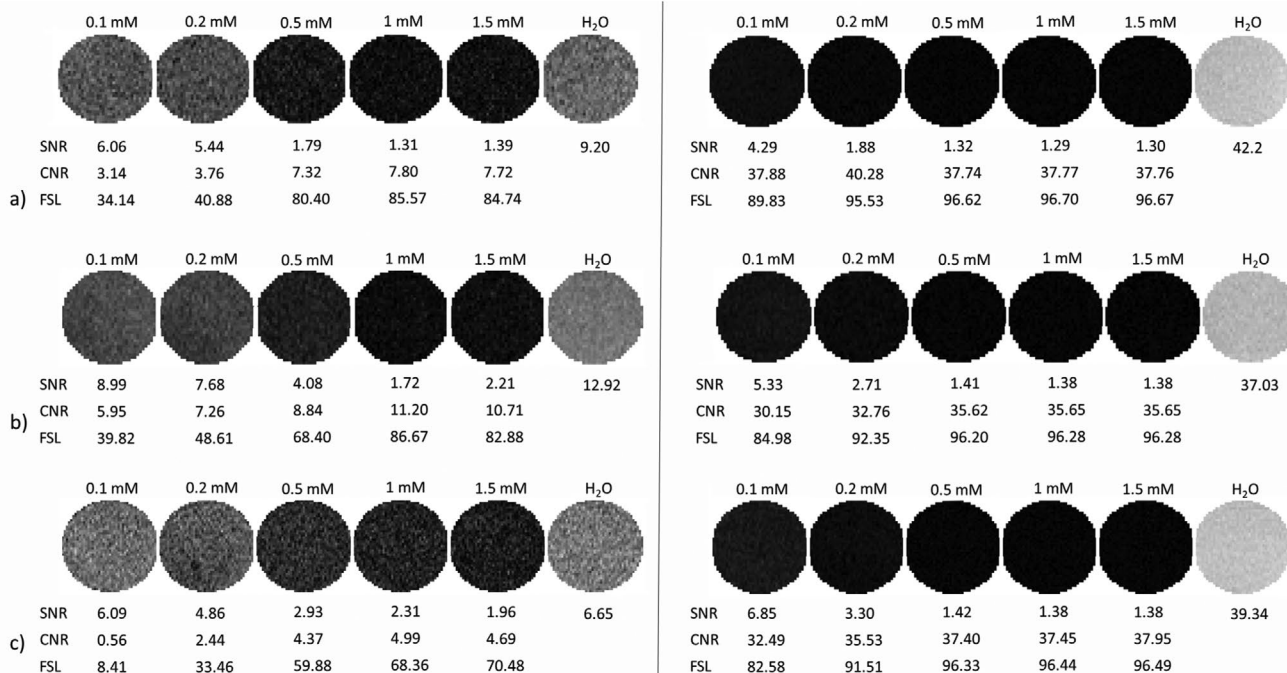
Figure 5. T_1 (left side) and T_2 weighted (right side) MR images of a) the Fe_3O_4 nanoclusters, b) the drug free $PEG-NH_2@Fe_3O_4-ZIF-8$, and c) the drug-loaded $PEG-NH_2@As@Fe_3O_4-ZIF-8$ nanoparticles with different concentrations of Fe ($0.1–1.5 \times 10^{-3}$ M). Corresponding SNR, CNR, and FSL values for given phantoms are shown.

Fe_3O_4 nanocluster was 48.51, and thus could be assigned as a "negative" contrast agent.[54] The drug free $PEG-NH_2@Fe_3O_4$-ZIF-8 and the drug-loaded $PEG-NH_2@As@Fe_3O_4$-ZIF-8 nanoparticles exhibited a r_2/r_1 ratio of 10.67 and 12.39, respectively, and also provided a very good contrast in MRI (Figure 5).

2.3. Drug Release and Stability Studies

The arsenic-release kinetics were investigated in a phosphate buffered saline of two different pH values (pH 6.0 and pH 7.4) at 37 °C in order to mimic the microenvironment of tumorous and healthy tissues.[55] After 1, 4, 6, 24, 48, 72, and 168 h the amount of arsenic, iron, and zinc released into the solution was determined by ICP-OES (**Figure 6**, Figures S8 and S9, and Tables S3–S5, Supporting Information).
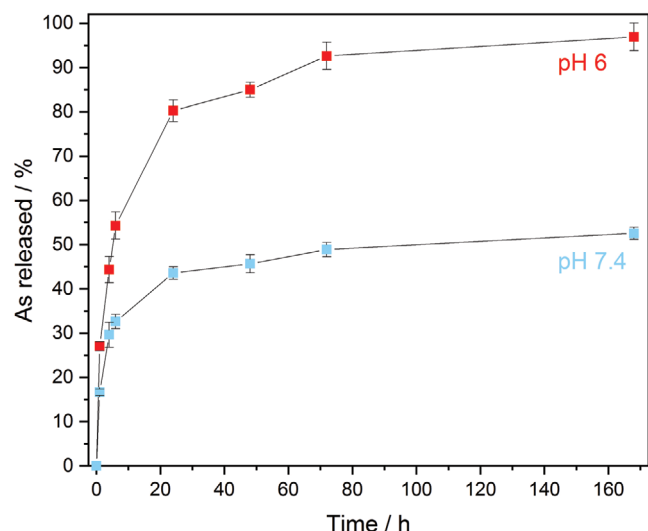
At pH 7.4 (normal tissue environment) 16.6% of arsenic was released after 1 h, 43.6% after 24 h and a maximum of 52.6% after 168 h. The burst drug release in the first few hours was not due to the MOF decomposition but due to the partial material disintegration as observed by XRPD, FT-IR, and STEM analyses

(Figures S10–S12, Supporting Information). The results of XRPD analyses revealed that the intensities corresponding to the ZIF-8 shell decreased progressively during the release studies. However, the total amount of zinc released to the phosphate buffered saline was less than 1% (Figure S8 and Table S3, Supporting Information) and since no formation of zinc salts was detected by XRPD, the decreased signal intensity of ZIF-8 most likely results from a progressive amorphisation of the framework. This was further confirmed by STEM analysis which revealed that after 4 h, the continuous ZIF-8 shell disintegrated into smaller nanoparticles located around the Fe_3O_4 core with a mean particle size of 15.8 ± 3.5 nm (Figure S10, Supporting Information). These remained unchanged during the rest of the release studies and did not decompose further. Thus, we suggest that the significantly higher external surface area of those small arsenic-loaded ZIF-8 nanoparticles, which was consequently exposed to the phosphate buffered saline, was the reason for the promoted arsenic release within the first few hours of the release studies. Once the surface bound drug was released, the release did not progress due to the material amorphisation. Therefore, to avoid the premature release, one possibility would be to pre-expose the material to the phosphate buffered saline before the administration.

At pH 6.0 a different drug release behavior was observed. 27.2% of arsenic was released already after 1 h, 80.2% after 24 h, and after 168 h all the amount of the originally loaded arsenic could be detected in the solution (Figure 6). This rapid and complete arsenic release was caused by the entire decomposition of the ZIF-8 shell at pH 6 which was accompanied by a progressive formation of $NaZn(PO_4)\cdot 4H_2O$ from the released zinc ions and phosphate anions of the buffer. The complete

Table 1. Relaxometric properties of Fe_3O_4 nanoclusters, drug free $PEG-NH_2@Fe_3O_4-ZIF-8$ and drug-loaded $PEG-NH_2@As@Fe_3O_4-ZIF-8$ measured at 1.5 T at 37 °C.

	r_1 [$\times 10^{-3}$ M^{-1} s^{-1}]	r_2 [$\times 10^{-3}$ M^{-1} s^{-1}]	r_2/r_1
Fe_3O_4	3.11	150.70	48.51
$PEG-NH_2@Fe_3O_4-ZIF-8$	2.37	25.25	10.67
$PEG-NH_2@As@Fe_3O_4-ZIF-8$	0.76	9.46	12.39

**ADVANCED
SCIENCE NEWS**

www.advancedsciencenews.com

Particle
& Particle Systems Characterization

www.particle-journal.com

Figure 6. Arsenic-release from PEG-NH$_2$@As@Fe$_3$O$_4$-ZIF-8 at pH 6 (red) and pH 7.4 (blue) in a phosphate buffered saline at 37 °C, determined by ICP-OES.

framework decomposition was verified by XRPD, FT-IR, and STEM analyses (Figures S13–S15, Supporting Information).

In addition to the ZIF-8 stability, also the stability of the Fe$_3$O$_4$ core was investigated by measuring the amount of iron released into the solution at pH 6 and pH 7.4 (Figure S9 and Table S4, Supporting Information). For both pH values, the detected amount of iron was below 1% during the entire release studies indicating that the Fe$_3$O$_4$ core did not decompose during the drug release studies.

2.4. Cytotoxicity Studies

To evaluate the cytotoxic effects of the core–shell nanoparticles, both drug-loaded (PEG-NH$_2$@As@Fe$_3$O$_4$-ZIF-8) and drug free nanocarriers (PEG-NH$_2$@Fe$_3$O$_4$-ZIF-8) were analyzed. We selected fibroblasts as non-tumorous cells and two different atypical teratoid rhabdoid tumor (ATRT) cell lines, namely BT12 and BT16, which are known to respond positively to ATO treatment,[48] and incubated them with the tested materials in a concentration range of 0.0001–100 × 10^{-6} M for 24 h and 72 h. The amount of the administrated substances was calculated with respect to the constant As- or Zn-amount (Table S5, Supporting Information). After the incubation time, cell viability was measured performing a MTT assay.[56]

The treatment of fibroblasts with the drug free nanocarrier (PEG-NH$_2$@Fe$_3$O$_4$-ZIF-8) showed that its cytotoxic effect was negligible for concentrations equal or lower than 10 × 10^{-6} M (Figure S16, Supporting Information). For higher concentrations, the cell viability decreased significantly. In the next step we analyzed the cell viability of fibroblasts treated with the drug-loaded nanoparticles (PEG-NH$_2$@As@Fe$_3$O$_4$-ZIF-8) after 24 h and 72 h (Figure S16, Supporting Information). For concentrations up to 1 × 10^{-6} M, the fraction vital fibroblasts after 72 h of incubation was similar or only slightly lower than that of PEG-NH$_2$@Fe$_3$O$_4$-ZIF-8. However, for concentrations equal or higher than 10 × 10^{-6} M, the cell viability decreased

noticeably. As shown in the stability studies, the core–shell nanoparticles partially disintegrated at pH 7.4 within the first 24 h and consequently some of the drug was released. We speculate that this drug release was most likely reflected in the decreased cell viability of the fibroblasts at the high administrated concentrations.

Subsequent to the studies with fibroblasts, the response of the ATRT cell lines BT12 and BT16 to the nanocarrier without and with the drug cargo was investigated. The results of PEG-NH$_2$@Fe$_3$O$_4$-ZIF-8 did not show any cytotoxic effects after 24 h for concentrations lower than 100 × 10^{-6} M on BT12 and BT16 cells (Figure S17, Supporting Information). The same results were obtained also after 72 h, even though the cell viability of BT16 cells was slightly unsteady for concentrations lower than 1 × 10^{-6} M (**Figure 7**a,b). In contrast to that, when testing the drug-loaded nanoparticles (PEG-NH$_2$@As@Fe$_3$O$_4$-ZIF-8), a clear cytotoxic effect was observed already after 24 h for
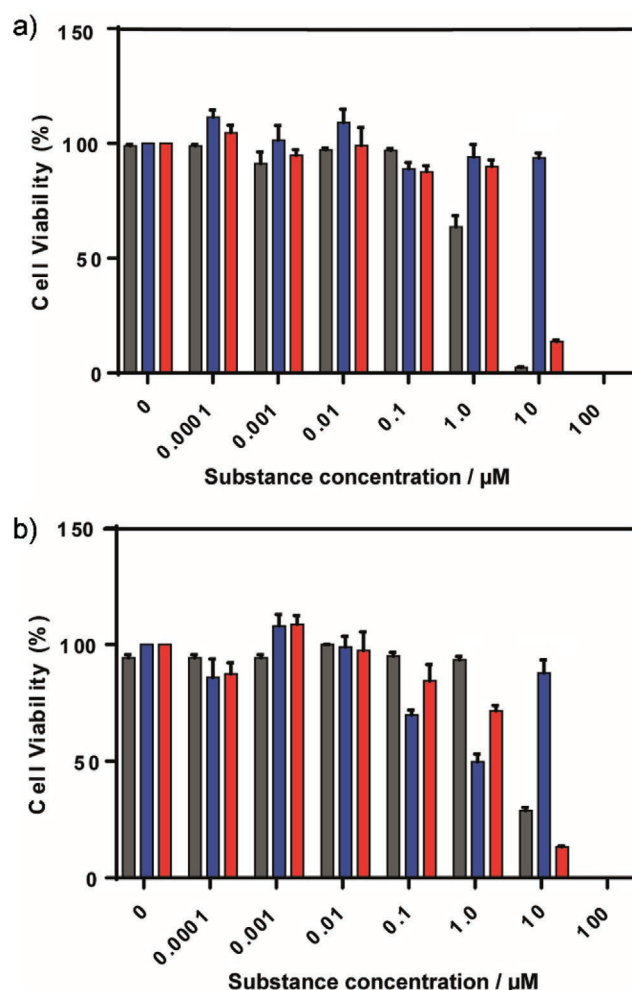
Figure 7. Cell viability of a) BT12 and b) BT16 cells after 72 h incubation with increasing concentrations of ATO (gray), PEG-NH$_2$@Fe$_3$O$_4$-ZIF-8 (blue), and PEG-NH$_2$@As@Fe$_3$O$_4$-ZIF-8 (red). The given concentration corresponds to the concentration of As$_2$O$_3$ (0–100 × 10^{-6} M) which was effectively loaded or could be theoretically loaded (for details see Table S5†, Supporting Information). Data are presented as mean ± S.E.M ($n \geq 3$). No cell viability was detected at 100 × 10^{-6} M after 72 h.

**ADVANCED
SCIENCE NEWS**
www.advancedsciencenews.com

Particle
& Particle Systems Characterization
www.particle-journal.com

Table 2. Half-maximal inhibitory concentrations (IC$_{50}$) values of selected materials after 72 h (the given IC$_{50}$ values correspond to the concentration of As$_2$O$_3$ which was effectively loaded or could be theoretically loaded).

IC$_{50}$ value [× 10^{-6} M] after 72 h	ATRT cell line.		Ref.
	BT12	BT16	
PEG-NH$_2$@Fe$_3$O$_4$-ZIF-8	28.0	20.5	This work
PEG-NH$_2$@As@Fe$_3$O$_4$-ZIF-8	3.3	2.0	This work
ATO	1.4	6.1	[44]
ZIF-8	12.5	12.8	[46]
PEG-NH$_2$@As@ZIF-8	2.4	2.1	[46]

concentrations higher than 1×10^{-6} M (Figure S17, Supporting Information). Herein, the cytotoxic effect was slightly more pronounced for BT12 cells than for BT16. This tendency was affirmed also after 72 h (Figure 7a,b). The comparison of the half maximal inhibitory concentration (IC$_{50}$) values in **Table 2** shows that the specific effect of arsenic-loaded PEG-NH$_2$@Fe$_3$O$_4$-ZIF-8 on both cancer cell lines is more than eight times higher than the effect of the nanocarrier itself.

Lastly, we compared the cytotoxic effect of the drug loaded nanocarrier to the effect caused by the free drug (ATO) after 24 h (Figure S17, Supporting Information) and 72 h (Figure 7a,b). Overall, we found that their cytotoxic effects were comparable. For concentrations higher than 1×10^{-6} M, the cytotoxic effect of ATO on BT12 was higher than the effect caused by the drug loaded nanoparticles (Figure 7a). However, in case of BT16 cells (Figure 7b), ATO caused a slightly lower cytotoxic effect than the drug loaded nanoparticles.

3. Conclusion

We successfully synthesized Fe$_3$O$_4$-ZIF-8 core–shell nanoparticles with an overall particle size below 100 nm. Such materials are attractive not only for medicinal applications but also for other areas of nanoscience including catalysis or extraction. Here we investigated their theragnostic potential: on the one hand as nanocarriers of arsenic trioxide (which was enabled by the porous MOF shell), on the other hand as contrast agents in MRI (which was enabled by the superparamagnetic Fe$_3$O$_4$ core). A SQUID measurement confirmed that the core–shell nanoparticles were superparamagnetic. Further, the results obtained by MR imaging affirmed that indeed the Fe$_3$O$_4$-ZIF-8 nanocarrier could be visualized by MRI. To demonstrate the drug delivery function, the MOF shell was loaded with arsenic trioxide. The drug was introduced to the framework via a post-synthetic ligand exchange with loading of 53 mg of arsenic per 1 g (equivalent to 70 mg of As$_2$O$_3$/1 g). The drug release was investigated in a phosphate buffered saline at two different pH values—7.4 and 6.0. At pH 6, the porous ZIF-8 shell decomposed rapidly and entirely while inducing a complete drug release. Whereas at pH 7.4, approximately only half of the loaded drug was released after 168 h. In addition, the results of the in vitro cytotoxicity studies showed that the drug free nanocarrier did not cause critical harm neither to the fibroblasts nor to the selected cancer cell lines at moderate concentrations. In case of

the drug-loaded nanoparticles, a substantial cytotoxic effect was observed on the cancer cell lines, while on fibroblast, a cytotoxic effect was detected only at higher concentrations. Thus, there was a considerable difference in the drug release and cytotoxicity in the different cell lines, and we could indeed observe a cell specific drug release, which is a highly desirable feature in cancer treatment. Inspired by the results, we encourage a further development and study of Fe$_3$O$_4$-MOF core–shell nanoparticles, and Fe$_3$O$_4$-ZIF-8 in particular, for theragnostic applications. For instance, we are currently working on combining the Fe$_3$O$_4$-ZIF-8 nanoparticles with targeting ligands and investigating their potential in cancer therapy.

4. Experimental Section

Materials and Methods: All reagents were of analytical grade and used as received from commercial suppliers: iron(III) chloride hexahydrate, anhydrous sodium acetate, trisodium citrate dihydrate, ethylene glycol, diethylene glycol, zinc nitrate hexahydrate, sodium (meta)arsenite, 2-methylimidazole and arsenic trioxide from Sigma-Aldrich, and alpha-monomethoxy-omega-amino poly(ethylene glycol) from Iris Biotech GmbH. Fourier transform infrared (FT-IR) spectra were recorded in the range of 400–4000 cm^{-1} on a Bruker Equinox 55 FT-IR spectrometer equipped with an ATR unit. Thermogravimetric analysis was measured on a TA Instruments Q500 device in a temperature range of 25–700 °C under a nitrogen atmosphere at a heating grade of 10 °C min^{-1}. X-ray powder diffraction data were collected in the 4–70° 2θ range using a Bruker D8 Advance diffractometer with Cu-K_α radiation ($\lambda = 1.54184$) with a 1D LynxEye detector. The samples were ground and filled into a Hilgenberg glass capillary (outer diameter 0.3 mm, wall thickness 0.01 mm). TEM micrographs and EDS elemental mappings were recorded with a JEM NEOARM microscope (JEOL) with a cold FEG electron source operated at 200 kV. SEM and STEM micrographs were recorded with a Crossbeam 550 Gemini II (ZEISS) with a FE-Gun operated at 30 kV. Samples were prepared by depositing a drop of the crystalline products dispersed in ethanol onto carbon-coated copper grids (200 mesh) and dried in air. The size of the nanoparticles was determined from calibrated TEM images using ImageJ software.[57] One hundred particles were analyzed to determine the average size. Dynamic light scattering (DLS) measurements were carried out using a Brookhaven 90Plus Nanoparticle Size Analyzer. Nanoparticles were dispersed in water prior the measurement. The elemental composition of solid and liquid samples was determined by ICP-OES with the Vista MPX of VARIAN with arsenic, iron, and zinc standard solution of 10 and 20 ppm. The samples were decomposed or diluted in an aqueous solution of HNO$_3$ prior to the measurement. CHN-elemental analysis was measured with a Vario EL III (Elementar-Analysensysteme GmbH). Cells were cultivated in a Heracell 150i CO$_2$ incubator (Thermo Scientific). MTT assay was analyzed using a Multiskan Ascent Microplate Reader (Thermo Electron Corporation). Magnetization loops M(H) as a function of the external magnetic field H were recorded with a Quantum Design MPMS 5 SQUID magnetometer at constant temperature in a field range between −50 and +50 kOe.

Synthesis of Fe$_3$O$_4$ Nanoclusters: FeCl$_3$·6H$_2$O (3.468 g), anhydrous sodium acetate (7.68 g) and trisodium citrate dihydrate (2.08 g) were dissolved in a mixture in 40 mL of ethylene glycol and 120 mL of diethylene glycol. Then the solution was stirred for 1 h at 120 °C (N$_2$-atm), transferred to a Teflon-lined stainless-steel autoclave (200 mL capacity) and heated at 200 °C for 10 h. The product was separated by using an external magnetic field and washed well with ethanol and deionized water. Finally, the nanoparticle clusters were dispersed in 100 mL of distilled water to store them.

Synthesis of Fe$_3$O$_4$-ZIF-8 Nanoparticles: To 17 mg of the Fe$_3$O$_4$ nanoclusters dispersed in 1.6 mL of distilled water and 5 mL of methanol, 2-methylimidazole (850 mg, 0.01 mol) dissolved in 25 mL

**ADVANCED
SCIENCE NEWS**

www.advancedsciencenews.com

Particle
& Particle Systems Characterization

www.particle-journal.com

of methanol was added. The mixture was ultrasonicated for 15 min, mixed with a solution of $Zn(NO_3)_2 \cdot 6H_2O$ (89 mg, 0.5 mmol) in 10 µL of distilled water and 10 mL of methanol and kept at room temperature for 30 min. After further 15 min of applying an external magnetic field, the material was washed with methanol (3 × 20 mL).

Drug Loading: An aqueous solution of sodium (meta)arsenite solution (7.7×10^{-3} M) of pH 7 was prepared by dissolving sodium (meta)arsenite $NaAsO_2$ (1 g, 7.7 mmol) in 1 L of distilled water and subsequent adjustment of the pH with 1 M hydrochloric acid. 45 mg of the prepared Fe_3O_4-ZIF-8 nanoparticles were dispersed in 16 mL of distilled water and 8 mL of the freshly prepared 7.7×10^{-3} M aqueous arsenite solution and kept at room temperature for 2 h. The material was isolated by applying an external magnetic field for 30 min, washed with deionized water (3 × 20 mL) and dried under ambient pressure at 75 °C.

Coating Nanoparticles with Amino-Functionalized Polyethylene Glycol: 45 mg of the drug free or loaded Fe_3O_4-ZIF-8 nanoparticles were dispersed in 5 mL of a 1.6×10^{-3} M aqueous solution of alpha-monomethoxy-omega-amino poly(ethylene glycol) ($PEG-NH_2$) and kept at room temperature. After 2 h the respective sample was placed into an external magnetic field for 30 min, washed with deionized water (3 × 20 mL) and dried under ambient pressure at 75 °C. The drug free ($PEG-NH_2@Fe_3O_4$-ZIF-8) and drug loaded ($PEG-NH_2@As@Fe_3O_4$-ZIF-8) materials were characterized by XRPD, FT-IR, TGA, TEM, ICP-OES, CHN-elemental analysis, EDS elemental mapping, SQUID, and in vitro MRI.

MR Imaging and Relaxometry: T_1 and T_2 weighted MR images of the phantoms containing the nanoparticles were acquired on a 4.7 T Bruker Biospec scanner using a resonator coil (Bruker, Biospin, Germany). A standard 2D rapid acquisition with relaxation enhancement (RARE) multi-spin echo MR sequence with spatial resolution 141 × 141 µm², and slice thickness of 1 mm was used. Following parameters of MR sequence were used: T_1 weighted MR images acquisition: TR = 300 ms, TE = 1.6 ms, turbo factor = 1; for T_2 MR weighted images acquisition: TR = 3000 ms, TE = 50 ms, turbo factor = 2. MR image processing and quantification were performed using ImageJ software.[57] The signal-to-noise ratio (SNR) was calculated using SNR = 0.655 S/σ equation, where S is signal intensity in the region of interest, σ is the standard deviation of background noise and constant 0.655 reflects the Rician distribution of background noise in a magnitude MR image. The contrast-to-noise ratio (CNR) was calculated as the difference in SNR between phantom and water. The fractional signal loss (FSL) was calculated as percentage signal drop in phantoms related to the water signal intensity.

The relaxivity of nanoparticles was measured on a 1.5 T Minispec 60 MHz relaxometer (Bruker Biospin, Germany) at stabilized temperature of 37 °C during the whole experiment. T_1 relaxation times were measured with the inversion recovery sequence (repetition time (TR) = 0.01–10 000 ms, recycle delay = 2 s, scans = 4, echo time (TE) = 0.05 ms, 20 points for fitting). T_2 relaxation times were measured with Carr–Purcell–Meiboom–Gill sequence (TR = 10 000 ms, recycle delay = 2 s, scans = 8, TE = 0.05 ms, 20 000 points for fitting). The relaxivities $r_{1,2}$ were calculated through the least-squares curve fitting of R_1, R_2 relaxation rates [s^{-1}] versus iron concentration [$\times 10^{-3}$ M]. To prevent sedimentation of nanoparticles during the measurement ($t = 5$ min), samples were fixed in 1% agar solution.

Drug Release: 10 mg of $PEG-NH_2@As@Fe_3O_4$-ZIF-8 were dispersed in 10 mL of 0.01 M phosphate buffered saline of pH 7.4 or 6.0. At a certain period of time (after 1, 4, 6, 24, 48, 72, or 168 h), 1 mL of the solution was removed for analysis and replaced by 1 mL of a fresh phosphate buffer solution. The amount of arsenic, iron, and zinc in the taken 1 mL of the sample was determined by ICP-OES analysis. The release studies were done in triplicates and the data are presented as mean ± standard deviation. Moreover, the remained nanoparticles after 4, 24, and 168 h were analyzed by XRPD, IR, STEM, and ICP-OES analyses.

Cell Culture: ATRT cell lines were cultured as suspension cells in NSC growth medium (DMEM/F12/Ham medium supplemented with B27 supplement (2%), N_2 supplement (1%), penicillin and streptomycin (1%), recombinant EGF (20 ng mL^{-1}) and recombinant FGF (20 ng mL^{-1}). BT12 cells were received from Dr. Marc Remke (University

of Düsseldorf, Germany) and BT16 cells from Dr. Martin Hasselblatt (University of Münster, Germany). Fibroblasts were provided by Niki Loges (University of Münster, Germany). All cells were cultured in 5% CO_2 at 37 °C. All cell lines were authenticated by STR-PCR profiling and regularly tested for mycoplasma.

Cytotoxicity Studies: Cells were seeded in a 96-well plate at a density of 4000 (fibroblasts), 4000 (BT16), or 8000 (BT12) cells per well. After 24 h, cells were treated with increasing concentrations (concentration range 0–100 × 10^{-6} M, calculated with respect to the constant As- or Zn-amount) of $PEG-NH_2@Fe_3O_4$-ZIF-8, $PEG-NH_2@As@Fe_3O_4$-ZIF-8, or ATO and incubated for 24 or 72 h. On the day of measurement, 10 µL of MTT reagent was added. Viable cells were converted tetrazolium dye MTT (3-(4,5-dimethylthiazol-2-yl)-2,5-diphenyltetrazolium bromide) into an insoluble, purple-colored formazan dye. After 3 h incubation time, formazan crystals were resuspended with 100 µL of isopropanol–HCl (0.04 N). MTT assay[52] was performed using a Multiskan Ascent Microplate Reader (Thermo Electron Corporation). The absorbance was measured at a wavelength of 570 nm and a reference wavelength of 630 nm. Data were analyzed using GraphPad Prism software version 7.00.

Supporting Information

Supporting Information is available from the Wiley Online Library or from the author.

Conflict of Interest

The authors declare no conflict of interest.

[1] J. Zhang, L. Ning, J. Huang, C. Zhang, K. Pu, *Chem. Sci.* **2020**, *11*, 618.

[2] E.-K. Lim, T. Kim, S. Paik, S. Haam, Y.-M. Huh, K. Lee, *Chem. Rev.* **2015**, *115*, 327.

[3] R. Kumar, W. S. Shin, K. Sunwoo, W. Y. Kim, S. Koo, S. Bhuniya, J. S. Kim, *Chem. Soc. Rev.* **2015**, *44*, 6670.

[4] J. H. Ryu, S. Lee, S. Son, S. H. Kim, J. F. Leary, K. Choi, I. C. Kwon, *J. Controlled Release* **2014**, *190*, 477.

[5] F. R. Vogenberg, C. Isaacson Barash, M. Pursel, *Pharmacol. Ther.* **2010**, *35*, 560.

[6] Y.-X. J. Wang, *Quant. Imaging Med. Surg.* **2011**, *1*, 35.

[7] J. Estelrich, E. Escribano, J. Queralt, M. Busquets, *Int. J. Mol. Sci.* **2015**, *16*, 8070.

[8] K. Ulbrich, K. Holá, V. Šubr, A. Bakandritsos, J. Tuček, R. Zbořil, *Chem. Rev.* **2016**, *116*, 5338.

[9] Y. Hu, S. Mignani, J.-P. Majoral, M. Shen, X. Shi, *Chem. Soc. Rev.* **2018**, *47*, 1874.

[10] Y.-X. J. Wang, S. Xuan, M. Port, J.-M. Idee, *Curr. Pharm. Des.* **2013**, *19*, 6575.

[11] G. Prabha, V. Raj, *J. Magn. Magn. Mater.* **2016**, *408*, 26.

[12] P. M. Price, J. W. Dittmar, K. Carlson, B. P. Lawson, A. K. Reilly, B. D. Stein, H. Cheng, O. Zholobko, A. Kohut, A. Voronov, L. M. Bronstein, *Part. Part. Syst. Charact.* **2019**, *36*, 1900112.

[13] S. Jiang, M. Mottola, S. Han, R. Thiramanas, R. Graf, I. Lieberwirth, V. Mailänder, D. Crespy, K. Landfester, *Part. Part. Syst. Charact.* **2020**, *37*, 1900484.

[14] G. Zhang, J. Gao, J. Qian, D. Cai, K. Zheng, Z. Yu, J. Wang, K. Zhong, X. Zhang, Z. Wu, *Part. Part. Syst. Charact.* **2014**, *31*, 976.

[15] Y.-S. Huang, Y.-J. Lu, J.-P. Chen, *J. Magn. Magn. Mater.* **2017**, *427*, 34.

[16] S. R. Batten, N. R. Champness, *Philos. Trans. R. Soc., A* **2017**, *375*, 20160032.

[17] O. M. Yaghi, M. O'Keeffe, N. W. Ockwig, H. K. Chae, M. Eddaoudi, J. Kim, *Nature* **2003**, *423*, 705.

[18] S. Yuan, L. Feng, K. Wang, J. Pang, M. Bosch, C. Lollar, Y. Sun, J. Qin, X. Yang, P. Zhang, Q. Wang, L. Zou, Y. Zhang, L. Zhang, Y. Fang, J. Li, H.-C. Zhou, *Adv. Mater.* **2018**, *30*, 1704303.

[19] H. Li, K. Wang, Y. Sun, C. T. Lollar, J. Li, H.-C. Zhou, *Mater. Today* **2018**, *21*, 108.

[20] J. Ren, H. W. Langmi, B. C. North, M. Mathe, *Int. J. Energy Res.* **2015**, *39*, 607.

[21] M. Liu, J. Wu, H. Hou, *Chem. - Eur. J.* **2019**, *25*, 2935.

[22] Y.-B. Huang, J. Liang, X.-S. Wang, R. Cao, *Chem. Soc. Rev.* **2017**, *46*, 126.

[23] L. Zhu, X.-Q. Liu, H.-L. Jiang, L.-B. Sun, *Chem. Rev.* **2017**, *117*, 8129.

[24] P. Horcajada, R. Gref, T. Baati, P. K. Allan, G. Maurin, P. Couvreur, G. Férey, R. E. Morris, C. Serre, *Chem. Rev.* **2012**, *112*, 1232.

[25] J. Yang, Y.-W. Yang, *Small* **2020**, *16*, 1906846.

[26] J. W. M. Osterrieth, D. Fairen-Jimenez, *Biotechnol. J.* **2020**, 2000005.

[27] K. S. Park, Z. Ni, A. P. Côté, J. Y. Choi, R. Huang, F. J. Uribe-Romo, H. K. Chae, M. O'Keeffe, O. M. Yaghi, *Proc. Natl. Acad. Sci. U. S. A.* **2006**, *103*, 10186.

[28] B. Chen, Z. Yang, Y. Zhu, Y. Xia, *J. Mater. Chem. A* **2014**, *2*, 16811.

[29] H. Zhang, Q. Li, R. Liu, X. Zhang, Z. Li, Y. Luan, *Adv. Funct. Mater.* **2018**, *28*, 1802830.

[30] Q. Yang, Q. Xu, H.-L. Jiang, *Chem. Soc. Rev.* **2017**, *46*, 4774.

[31] F. Pang, M. He, J. Ge, *Chem. - Eur. J.* **2015**, *21*, 6879.

[32] G. Zhao, N. Qin, A. Pan, X. Wu, C. Peng, F. Ke, M. Iqbal, K. Ramachandraiah, J. Zhu, *J. Nanomater.* **2019**, 1454358.

[33] M. Aghayi-Anaraki, V. Safarifard, *Eur. J. Inorg. Chem.* **2020**, *2020*, 1916.

[34] G. Chen, B. Yu, C. Lu, H. Zhang, Y. Shen, H. Cong, *CrystEngComm* **2018**, *20*, 7486.

[35] F. Ke, L.-G. Qiu, Y.-P. Yuan, X. Jiang, J.-F. Zhu, *J. Mater. Chem.* **2012**, *22*, 9497.

[36] H.-X. Zhao, Q. Zou, S.-K. Sun, C. Yu, X. Zhang, R.-J. Li, Y.-Y. Fu, *Chem. Sci.* **2016**, *7*, 5294.

[37] J. Lin, P. Xin, L. An, Y. Xu, C. Tao, Q. Tian, Z. Zhou, B. Hu, S. Yang, *Chem. Commun.* **2019**, *55*, 478.

[38] X. Zhou, W. Zhao, M. Wang, S. Zhang, Y. Li, X. Hu, R. Lei, S. Luo, Z. Chen, *ACS Appl. Mater. Interfaces* **2020**, *12*, 32278.

[39] W. H. de Jong, P. J. A. Borm, *Int. J. Nanomed.* **2008**, *3*, 133.

[40] E. P. Swindell, P. L. Hankins, H. Chen, D. U. Miodragović, T. V. O'Halloran, *Inorg. Chem.* **2013**, *52*, 12292.

[41] European Medical Agency (EMA), Trisenox EMEA/H/C000388/II/0058 assessment report, **2016**.

[42] R. W. Ahn, F. Chen, H. Chen, S. T. Stern, J. D. Clogston, A. K. Patri, M. R. Raja, E. P. Swindell, V. Parimi, V. L. Cryns, T. V. O'Halloran, *Clin. Cancer Res.* **2010**, *16*, 3607.

[43] Y. Du, D. Zhang, H. Liu, R. Lai, *BMC Biotechnol.* **2009**, *9*, 84.

[44] K. Kerl, N. Moreno, T. Holsten, J. Ahlfeld, J. Mertins, M. Hotfilder, M. Kool, K. Bartelheim, S. Schleicher, R. Handgretinger, U. Schüller, M. Meisterernst, M. Frühwald, *Int. J. Cancer* **2014**, *135*, 989.

[45] A. Akhtar, S. Xiaoyan Wang, L. Ghali, C. Bell, X. Wen, *J. Biomed. Res.* **2017**, *31*, 177.

[46] R. Ettlinger, M. Sönksen, M. Graf, N. Moreno, D. Denysenko, D. Volkmer, K. Kerl, H. Bunzen, *J. Mater. Chem. B* **2018**, *6*, 6481.

[47] J. Schnabel, R. Ettlinger, H. Bunzen, *ChemNanoMat* **2020**, *6*, 1229.

[48] R. Ettlinger, N. Moreno, D. Volkmer, K. Kerl, H. Bunzen, *Chem. - Eur. J.* **2019**, *25*, 13189.

[49] M. Wu, X. Guo, F. Zhao, B. Zeng, *Sci. Rep.* **2017**, *7*, 8912.

[50] F. Xu, C. Cheng, D.-X. Chen, H. Gu, *ChemPhysChem* **2012**, *13*, 336.

[51] H. A. Szymanski, L. Marabella, J. Hoke, J. Harter, *Appl. Spectrosc.* **1968**, *22*, 297.

[52] J. Wang, J. Sun, Q. Sun, Q. Chen, *Mater. Res. Bull.* **2003**, *38*, 1113.

[53] S.-L. Cao, H. Xu, L.-H. Lai, W.-M. Gu, P. Xu, J. Xiong, H. Yin, X.-H. Li, Y.-Z. Ma, J. Zhou, M.-H. Zong, W.-Y. Lou, *Bioresour. Bioprocess.* **2017**, *4*, 56.

[54] Y.-M. Huh, Y.-W. Jun, H.-T. Song, S. Kim, J.-S. Choi, J.-H. Lee, S. Yoon, K.-S. Kim, J.-S. Shin, J.-S. Suh, J. Cheon, *J. Am. Chem. Soc.* **2005**, *127*, 12387.

[55] I. F. Tannock, D. Rotin, *Cancer Res.* **1989**, *49*, 4373.

[56] T. Mosmann, *J. Immunol. Methods* **1983**, *65*, 55.

[57] C. T. Rueden, J. Schindelin, M. C. Hiner, B. E. DeZonia, A. E. Walter, E. T. Arena, K. W. Eliceiri, *BMC Bioinformatics* **2017**, *18*, 529.